arXiv:2608.21885v1 [cs.CV] 22 Aug 2026

Pixel-Space Diffusion via Observation Operators

Shaojie Guo[1], Lichen Ma[2,3], Haoyang Tong[2], Yu He[2], Zipeng Guo[2], Xiaoan Liu[2], Feng Yan[2], Yu Guo[2], Fei Wang[2], Junshi Huang[2], Yan Wang[1]

[1]East China Normal University
[2]JD.com
[3]State Key Laboratory of Human-Machine Hybrid Augmented Intelligence, Institute of Artificial Intelligence and Robotics, Xi'an Jiaotong University

Abstract

Pixel-space diffusion models directly model image distributions but remain difficult to optimize. Recent methods alleviate this challenge through target reparameterization, while still relying on a fixed clean-image target throughout denoising. Through empirical analysis, we identify a scale–time mismatch: image structures become predictable from coarse to fine as noise decreases, whereas existing models are forced to predict the full image even under high noise, resulting in low-SNR gradients that hinder optimization. To resolve this mismatch, we propose Observation Operator Diffusion, a unified framework that aligns both the supervision trajectory and feature refinement with the intrinsic recovery order of image structures. Specifically, we replace fixed full-image supervision along the standard flow path with a time-indexed observation trajectory that evolves from coarse structures to the full image during denoising. This trajectory is instantiated with a family of Gaussian–Lanczos operators at varying observation scales, yielding a path-consistent training objective. We further introduce GL-CoDA, a decoder that injects scale-specific Gaussian–Lanczos observations across decoding stages for coarse-to-fine feature refinement. Extensive experiments show that the proposed approach converges substantially faster while consistently improving generation quality, achieving an FID of 1.52 on ImageNet-256.

Introduction

Pixel-space diffusion has recently regained attention (Li and He 2025). Unlike latent diffusion (Rombach et al. 2022), which generates within a compressed representation, it models images directly in pixel space. This avoids information loss from autoencoder compression and reconstruction errors introduced by a fixed decoder, providing a direct route to high-fidelity generation (Chen et al. 2025; Yu et al. 2026). However, this advantage comes with substantially greater optimization difficulty (Chen et al. 2026a).

Recent studies show that optimization depends critically on the prediction target: even at a fixed pixel dimensionality, target reparameterization can markedly accelerate convergence (Li and He 2025), motivating increasing attention to target design (Chen et al. 2026a; Jin and Wang 2026). However, these methods change only the target parameterization while retaining the full image supervision throughout denoising. This distinction is particularly important in pixel space. Unlike latent-space models, where a compressed target delegates image reconstruction to a decoder, pixel-space models must directly predict image structures spanning multiple scales, from global layout to local textures. Yet the recoverability of these structures changes continuously with noise level: coarse structures emerge earlier, while fine details become predictable only as noise decreases (Fig. 1). Full-image supervision therefore forces the model to fit unrecoverable fine details at early denoising stages. We term this discrepancy between the fixed supervised scale and the time-dependent recoverable scale a scale–time mismatch, and identify it as a fundamental yet under-recognized source of optimization difficulty in pixel-space diffusion.

Copyright © 2027, Association for the Advancement of Artificial Intelligence (www.aaai.org). All rights reserved.

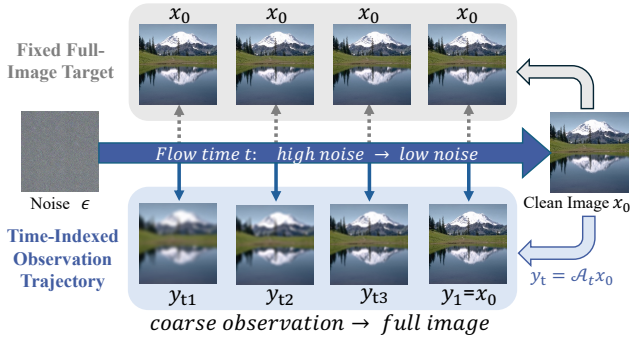

Figure 1: **Fixed full-image supervision vs. time-indexed observation trajectory.** Existing pixel-space diffusion models use the full clean image x_0 as the target throughout the denoising path. We instead introduce a time-indexed observation trajectory $y_t = \mathcal{A}_t(x_0)$, whose image content evolves from coarse structure to the full image as denoising proceeds.

To substantiate this claim, we measure prediction errors across spatial scales throughout denoising (Fig. 2; measurement protocol in the Appendix). The results reveal a clear coarse-to-fine recovery order: under high noise, coarse structures can already be reliably inferred, while fine details remain ambiguous and become recoverable only as noise decreases. This behavior is misaligned with the fixed full-image supervision used by existing pixel-space models, which requires the network to predict uncertain fine details even at high noise levels. Such a scale–time mismatch introduces low-SNR supervision signals, reducing the efficiency of optimization and ultimately slowing convergence (Fig. 3).

A natural solution is to supervise pixel-space models only

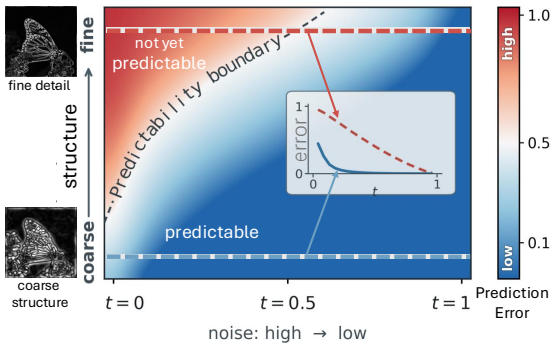

Figure 2: **Scale-dependent predictability during denoising.** We decompose the single-step prediction residual into multiscale structural bands and measure the prediction error at each scale. The heatmap (denoising time × spatial scale) and representative trajectories (inset) show that coarse structures become recoverable earlier than fine details, exposing the mismatch with fixed full-image supervision.

on the image structures that are predictable at the current noise level, rather than on the full image throughout denoising. The prediction target should therefore evolve with flow time, following the coarse-to-fine order in which image structures become recoverable. Building on this idea, we propose Observation Operator Diffusion, which replaces the fixed full-image target in the standard flow path with a time-indexed observation trajectory. We instantiate this trajectory with separable Gaussian–Lanczos operators, whose controllable scale selectivity enables progressive coarse-to-fine supervision while suppressing ringing artifacts. By annealing their scales over time, the observations evolve smoothly from a coarse low-pass image to the full image. The existing full image path can be considered a special case when the observation operator is an identity operator.

We further derive a path-consistent objective to explicitly couple the supervision scale with flow time, ensuring that each noisy input is trained against only the image structures recoverable at its current noise level. At high noise levels, this prevents unresolved fine details from interfering with the learning target, producing higher-SNR gradients and accelerating convergence (Fig. 3). This coarse-to-fine principle is also extended from the evolution of supervision over time to the refinement of features across network depth. To this end, we introduce GL-CoDA, a Gaussian–Lanczos Coarse-to-Detail Aggregation decoder that injects scale-specific structural responses into decoding stages and progressively aggregates them from coarse to fine. In this way, the decoder follows a progressive refinement of the representation from the global structure to fine-grained details. Our contributions are summarized as follows:

- We reveal an overlooked source of optimization difficulty in pixel-space diffusion, termed *scale–time mismatch*, arising from the discrepancy between the coarse-to-fine structure recovery and fixed full-image supervision.
- We propose Observation Operator Diffusion, which replaces fixed full-image supervision with a time-indexed trajectory of Gaussian–Lanczos observations, and derive a path-consistent objective that aligns the supervised scale with the structure recoverable at each denoising step.
- We introduce GL-CoDA, a scale-ordered decoder that injects Gaussian–Lanczos responses across decoding stages, extending the coarse-to-fine principle to feature refinement over network depth.
- Extensive experiments demonstrate substantially faster convergence and consistently improved generation quality, achieving an FID of **1.52** on ImageNet-256.

Related Work

Pixel-Space Diffusion and Prediction Objectives. Pixel-space diffusion avoids the reconstruction bottleneck of latent autoencoders, but remains challenging to optimize (Ho, Jain, and Abbeel 2020; Dhariwal and Nichol 2021; Peebles and Xie 2023a). Recent pixel-space architectures improve this tradeoff through patch–pixel modeling, hyper-connected feature reuse, or U-shaped transformer designs (Yu et al. 2026; He et al. 2026; Guo et al. 2026). Recent studies have explored alternative prediction objectives to improve optimization. JiT adopts clean-image prediction to exploit the low-dimensional structure of natural images (Li and He 2025); Asymmetric Flow Models restrict noise prediction to a low-rank subspace while retaining full-dimensional data prediction (Chen et al. 2026a); and k-Diff adapts the prediction target according to data dimensionality (Jin and Wang 2026). Despite different parameterizations, they all retain full-image supervision throughout denoising. Our work instead considers the temporal evolution of structure recoverability and adapts the supervision scale accordingly, following the intrinsic coarse-to-fine recovery order of image structures.

Scale-Aware Pixel Diffusion. Several recent methods incorporate the multiscale nature of image generation into pixel-space diffusion. DeCo (Ma et al. 2026b) assigns low-frequency semantics and high-frequency details to different network components and introduces a frequency-aware loss. FREPix (Lin et al. 2026) decomposes generation into low- and high-frequency components with separate transport paths. Spectral Forcing (Fan et al. 2026) filters noisy inputs in the DCT domain to suppress high-frequency components dominated by noise. FrequencyBooster (Ma et al. 2026a) further strengthens pixel-space modeling with a high-capacity decoder for full-frequency detail recovery. Energy-Guided Flow Matching (Tong et al. 2026) replaces the fixed clean endpoint with an energy-scheduled moving endpoint to explicitly encode coarse-to-fine generation. These works highlight the importance of frequency and scale structure, while our method reformulates the supervision target itself as a continuous observation trajectory whose scale is explicitly coupled to diffusion time.

Scale-Space Representations and Image Operators. Scale-space theory models an image as a family of continuously indexed observations at different spatial scales (Witkin 1983; Lindeberg 1994). Related image operators, including Gaussian filters, Laplacian pyramids, and Lanczos kernels, have long been used to represent, analyze, and resample image content across spatial scales (Burt and Adelson 1983;

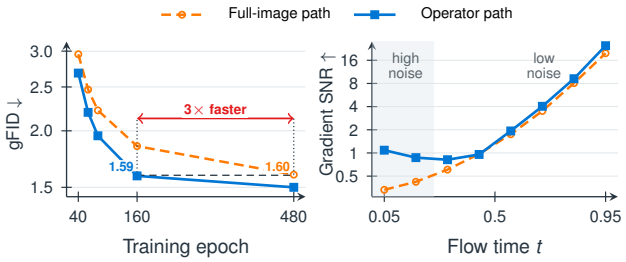

Figure 3: **Optimization benefits of the observation trajectory. Left:** Observation Operator Diffusion converges substantially faster than conventional full-image supervision while achieving a lower final FID. **Right:** Gradient signal-to-noise ratio (SNR) over diffusion time. By avoiding supervision of unresolved fine details, the observation trajectory maintains higher-SNR gradients in the high-noise regime, leading to more efficient optimization.

Turkowski 1990). The concept of using scale as an image representation attribute has been initially explored in diffusion models (Hoogeboom and Salimans 2022). Our method establishes this connection by constructing a diffusion-time-indexed family of Gaussian–Lanczos observations, turning spatial scale into a dynamic prediction target that evolves continuously throughout denoising.

Method

Figure 4 presents the proposed observation operator diffusion framework. Motivated by the empirically observed coarse-to-fine predictability during denoising, we replace the fixed full-image target with a time-indexed Gaussian–Lanczos observation trajectory and derive a path-consistent training objective. To extend the same coarse-to-fine principle to feature refinement, we further introduce a two-stage Patch–Pixel backbone with a GL-CoDA decoder, whose GL structure branch injects scale-specific structural responses across decoding stages. By jointly aligning supervision over denoising time and feature refinement over network depth, the proposed framework improves both optimization efficiency and generation quality.

Scale–Time Mismatch in Pixel-Space Diffusion

Recent pixel-space diffusion models are commonly trained using flow matching (Lipman et al. 2023). Given a clean image $x_0 \sim p_{\text{data}}$ and Gaussian noise $\epsilon \sim \mathcal{N}(0, I)$, flow matching defines the linear path

$$z_t = tx_0 + (1-t)\epsilon, \qquad t \in (0,1), \tag{1}$$

with target velocity $v_t^\star = \dot{z}_t = x_0 - \epsilon$. At each training iteration, the model takes the noisy state z_t, flow time t, and class condition c as input. For a prediction parameterization $\pi \in \{x, \epsilon, v\}$, the model produces

$$r_\theta^\pi = F_\theta^\pi(z_t, t, c). \tag{2}$$

Although these parameterizations predict different quantities, their prediction errors can be mapped to a common image space. Following the unified formulation of JiT (Li and He 2025), each direct prediction induces an estimate of the clean image:

$$\hat{x}_\theta^\pi = \begin{cases} r_\theta^x, & \pi = x, \\ \dfrac{z_t - (1-t)r_\theta^\epsilon}{t}, & \pi = \epsilon, \\ z_t + (1-t)r_\theta^v, & \pi = v, \end{cases} \qquad \pi \in \{x, \epsilon, v\}. \tag{3}$$

Let $\delta x_\theta^\pi = \hat{x}_\theta^\pi - x_0$ denote the corresponding image-space error. The standard mean-squared-error objective can be expressed in terms of this common image-space error as

$$\mathcal{L}_\pi = \mathbb{E}\left[w_\pi(t)\,\|\delta x_\theta^\pi\|_2^2\right], \qquad \pi \in \{x, \epsilon, v\}, \tag{4}$$

where $w_x(t) = 1$, $w_\epsilon(t) = t^2/(1-t)^2$, and $w_v(t) = 1/(1-t)^2$. Equations (3)–(4) show that, in the common image space, target reparameterization only introduces a timestep-dependent scalar weighting on the prediction error. Although different parameterizations emphasize different timesteps, they all evaluate the induced clean-image estimate against the same full-resolution target x_0. Since a scalar rescales the entire error uniformly, coarse structure and fine detail remain equally present in the training signal at every timestep.

This fixed supervision is misaligned with the coarse-to-fine order in which image structures become recoverable during denoising. As shown in Fig. 2, coarse structures can be reliably recovered well before fine details. Consequently, full-image supervision requires the model to fit fine details before they are reliably inferable from the noisy input, introducing low-SNR gradients at high noise levels. This scale–time mismatch reduces optimization efficiency, slowing convergence and ultimately degrading generation quality (Fig. 3).

Gaussian-Lanczos Observation Operator Path

To align the spatial content of supervision with the image structures that are reliably predictable at each flow time, we replace the fixed full-image target with a time-indexed observation trajectory. Specifically, we introduce a family of operators $\{\mathcal{A}_t : \mathbb{R}^{C\times H\times W} \to \mathbb{R}^{C\times H\times W}\}_{t\in[0,1]}$ and define

$$y_t = \mathcal{A}_t(x_0). \tag{5}$$

Each operator preserves the spatial resolution of the image while controlling the spatial scale of the observed content. We require the operator family to satisfy

$$\mathcal{A}_0 = \mathcal{A}_{\text{coarse}}, \qquad \mathcal{A}_1 = \mathcal{I}, \tag{6}$$

where $\mathcal{A}_{\text{coarse}}$ produces a coarse low-pass observation and $\mathcal{I}$ denotes the identity operator. Thus, the observation trajectory starts from coarse image structure and gradually recovers finer details, reaching the full clean image at $t = 1$: $y_0 = \mathcal{A}_{\text{coarse}}(x_0)$ and $y_1 = x_0$. To ensure that this trajectory is compatible with flow matching, we further require $t \mapsto \mathcal{A}_t(x)$ to be absolutely continuous for every image x. The resulting observation trajectory is therefore continuous and differentiable almost everywhere, so that its flow-matching velocity is well defined. Using y_t as a time-dependent prediction target we construct the observation path

$$z_t = t\,y_t + (1-t)\epsilon = t\,\mathcal{A}_t(x_0) + (1-t)\epsilon. \tag{7}$$

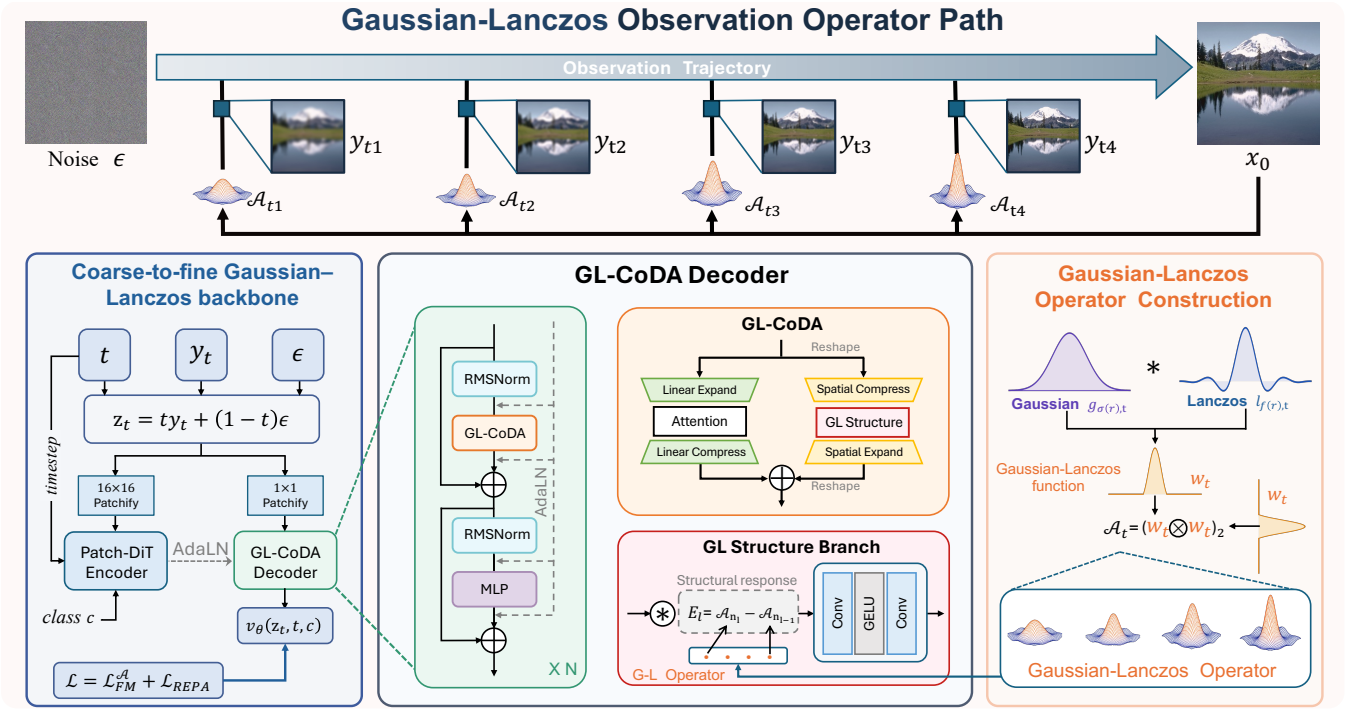

Figure 4: **Overview of the proposed Observation Operator Diffusion framework. Top:** Gaussian–Lanczos observation trajectory, where a family of operators $\mathcal{A}_t$ maps the clean image x_0 to time-indexed observations $y_t = \mathcal{A}_t(x_0)$, progressively transitioning from coarse structures to the full image along denoising. **Bottom:** two-stage Patch–Pixel backbone, comprising a Patch-DiT encoder and a GL-CoDA decoder. The GL structure branch injects scale-specific structural responses across decoding stages. The right panel details the construction of each Gaussian–Lanczos operator $\mathcal{A}_t$.

The path starts from pure noise, $z_0 = \epsilon$, and terminates at the clean image, $z_1 = y_1 = x_0$. Differentiating Eq. (7) with respect to flow time gives the path-consistent velocity target

$$v_t^\star = \dot{z}_t = y_t - \epsilon + t\,\dot{y}_t, \qquad \dot{y}_t = \partial_t \mathcal{A}_t(x_0). \tag{8}$$

Compared with the standard flow-matching target, the additional term $t\dot{y}_t$ captures the temporal evolution of the observation anchor. The network $F_\theta(z_t, t, c)$ directly predicts the resulting path-consistent velocity and is trained with

$$\mathcal{L}_{\mathrm{FM}}^{\mathcal{A}} = \mathbb{E}_{(x_0,c),\epsilon,t}\left[\|F_\theta(z_t,t,c) - v_t^\star\|_2^2\right]. \tag{9}$$

Relation to standard flow matching. When $\mathcal{A}_t \equiv \mathcal{I}$, the observation is fixed at $y_t = x_0$, giving $\dot{y}_t = 0$. Equations (7) and (8) then reduce to

$$z_t = tx_0 + (1-t)\epsilon, \qquad v_t^\star = x_0 - \epsilon, \tag{10}$$

which recovers the standard flow-matching path and velocity target. Thus, standard flow matching is recovered as the identity-operator special case of our framework.

Gaussian–Lanczos Operator Construction

Kernel construction. Let $\mathcal{R} = \{-R, \ldots, R\}$ denote the discrete kernel support. On this support, we define the Lanczos and Gaussian components as

$$\begin{aligned} h_f[r] &= \mathbf{1}_{\{|r|<2f\}}\,\mathrm{sinc}\left(\frac{r}{f}\right)\mathrm{sinc}\left(\frac{r}{2f}\right), \\ g_\sigma[r] &= \exp\left(-\frac{r^2}{2\sigma^2}\right), \qquad r \in \mathcal{R}, \end{aligned} \tag{11}$$

where $\mathrm{sinc}(a) = \sin(\pi a)/(\pi a)$ and $\mathrm{sinc}(0) = 1$. For the limiting case $\sigma = 0$, we define $g_0 := \delta_0$, with δ_0 denoting the discrete unit impulse. We then form the one-dimensional Gaussian–Lanczos kernel by

$$w_t = \mathcal{N}\big(\mathcal{N}(h_{f(t)}) *_R \mathcal{N}(g_{\sigma(t)})\big), \tag{12}$$

where $*_R$ denotes convolution restricted to the support $\mathcal{R}$ and $\mathcal{N}(\cdot)$ denotes kernel normalization. The corresponding separable two-dimensional kernel defines the observation operator as

$$\mathcal{A}_t = (w_t \otimes w_t) *_2, \tag{13}$$

where $\otimes$ denotes the outer product and $*_2$ denotes channel-wise two-dimensional convolution. The resulting observation is therefore

$$y_t = (w_t \otimes w_t) *_2 x_0. \tag{14}$$

The Gaussian and Lanczos components provide complementary properties: Lanczos filtering enables sharper scale selectivity, while Gaussian smoothing suppresses its ringing artifacts. As shown in Fig. 5(a), Gaussian smoothing attenuates the oscillatory sidelobes of the Lanczos kernel in the spatial domain. In the frequency domain, Fig. 5(b) shows that the combined kernel has a narrower transition band than Gaussian smoothing alone at the same $-3\,\mathrm{dB}$ cutoff, enabling sharper frequency selectivity.

Time-dependent scale schedule. We couple the kernel scales to flow time through

$$f(t) = 1 + (f_0 - 1)(1-t), \qquad \sigma(t) = \sigma_0(1-t), \tag{15}$$

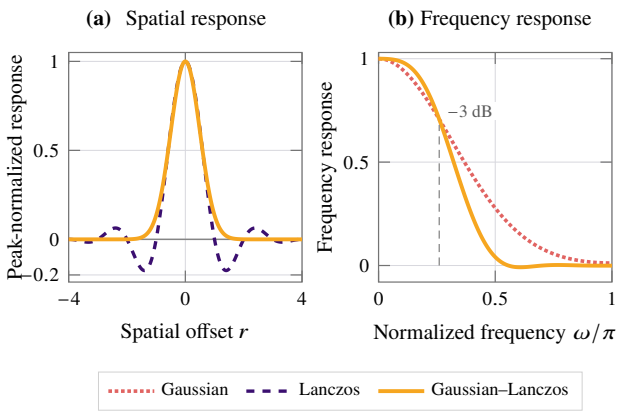

Figure 5: **Spatial and frequency responses of the Gaussian–Lanczos kernel.** *(a) Spatial response.* Gaussian smoothing attenuates the signed sidelobes of the Lanczos component, reducing potential ringing. *(b) Frequency response.* At a matched $-3\,\mathrm{dB}$ cutoff, the Gaussian–Lanczos kernel exhibits a narrower transition band than the Gaussian-only kernel, yielding sharper scale selectivity and stronger attenuation of high-frequency detail.

where $f_0 > 1$ and $\sigma_0 > 0$. As t increases, both $f(t)$ and $\sigma(t)$ decrease toward their identity-filtering limits. The resulting broader kernels at early times suppress fine-scale variations, while the progressively narrower kernels recover edges and textures as the path approaches the clean image.

At $t = 1$, the Gaussian component is defined by its discrete limit $g_0 = \delta_0$. Moreover, $f(1) = 1$, for which the sampled Lanczos kernel satisfies $h_1 = \delta_0$ on the integer grid. Hence, the endpoint kernel is obtained by continuous extension:

$$w_1 := \lim_{t \to 1^-} w_t = \delta_0, \qquad y_1 = \mathcal{A}_1(x_0) = x_0. \tag{16}$$

Thus, the observation trajectory continuously transitions from a coarse low-pass observation to exact clean image.

Path derivative. For $t \in (0, 1)$, the time derivative of the one-dimensional kernel follows from the chain rule:

$$\dot{w}_t = \frac{\partial w_t}{\partial f} \dot{f}(t) + \frac{\partial w_t}{\partial \sigma} \dot{\sigma}(t). \tag{17}$$

Differentiating the corresponding separable two-dimensional kernel then gives

$$\dot{y}_t = (\dot{w}_t \otimes w_t + w_t \otimes \dot{w}_t) *_2 x_0. \tag{18}$$

Because the Lanczos kernel is piecewise smooth due to its finite-support indicator, the derivative with respect to t exists almost everywhere, which is sufficient for the flow-matching objective. The resulting $\dot{y}_t$ induces the additional $t\dot{y}_t$ term in the path-consistent velocity target.

Coarse-to-Fine Gaussian–Lanczos Decoder

Pixel-space generation requires both global context modeling and spatially precise refinement. Following the two-stage Patch–Pixel design of PixelDiT, our backbone comprises a Patch-DiT encoder and a GL-CoDA decoder. The Patch-DiT encoder captures global semantics at the patch level, while the GL-CoDA decoder progressively refines the representation at the pixel level. Each GL-CoDA block contains an attention branch and a parallel *GL structure branch*. The former models long-range dependencies over a linearly compressed set of pixel tokens, while the latter injects Gaussian–Lanczos responses that progress from coarse to fine across decoder depth. This design extends the same scale-aware principle from the temporal evolution of supervision to the spatial refinement of network features.

Concretely, given the normalized pixel features h_l at the l-th GL-CoDA block, we first rearrange the pixel tokens into a full 2D feature map to restore their spatial adjacency. We then apply $2\times$ average pooling to suppress local noise and reduce computational cost, obtaining a spatially compressed feature map F_l. The structural operators reuse the Gaussian–Lanczos construction defined in Sec. . We assign four scales $\{n_1, \ldots, n_4\}$ to successive decoder blocks in coarse-to-fine order, with the finest-scale operator $\mathcal{A}_{n_4} = \mathcal{I}$. The structural response at the l-th block is

$$E_l = \begin{cases} \mathcal{A}_{n_1}(F_l), & l = 1, \\ \mathcal{A}_{n_l}(F_l) - \mathcal{A}_{n_{l-1}}(F_l), & l = 2, 3, 4. \end{cases} \tag{19}$$

The first block captures the coarse-scale structure, while subsequent blocks extract progressively finer structural increments by taking differences between adjacent operator responses. This adjacent-difference construction prevents redundant re-injection of coarse structures across decoder depths, allowing each block to provide complementary information at its designated scale. Each response is then refined by a lightweight adapter $\mathcal{P}_l$ and injected into the pixel representation produced by the attention branch:

$$\widetilde{h}_l = h_l^{\mathrm{attn}} + \mathcal{P}_l(E_l), \tag{20}$$

where $\mathcal{P}_l$ upsamples the response by $2\times$, reversing the earlier pooling operation, and rearranges it into the pixel-token space. The resulting residual injection preserves the full-resolution main stream while progressively enriching its local structure from coarse to fine.

Training Objective. We train the model with the proposed path-consistent flow-matching objective together with REPA representation alignment

$$\mathcal{L} = \mathcal{L}_{\mathrm{FM}}^{\mathcal{A}} + \mathcal{L}_{\mathrm{REPA}}. \tag{21}$$

In practice, we use direct v prediction and evaluate $\mathcal{L}_{\mathrm{FM}}^{\mathcal{A}}$ in v space due to its good optimization stability and generation performance.

Experiments

Evaluation setup. We conduct class-conditional generation experiments on ImageNet-1K (Deng et al. 2009) at 256^2 and 512^2 resolutions. Unless otherwise specified, all models and ablations are trained for 80 epochs. We evaluate generation quality using 50K generated samples and report Fréchet Inception Distance (FID) (Heusel et al. 2017), spatial FID (sFID), Inception Score (IS), precision, and recall.

Space	Method	Epochs	#params	gFID↓	sFID↓	IS↑	Precision↑	Recall↑
Latent	REPA (Yu et al. 2024)	800	675M	1.42	4.70	305.7	0.80	0.65
	SVG-XL (Shi et al. 2025)	1400	675M	1.92	–	264.9	–	–
	DDT-XL (Wang et al. 2025)	400	675M	1.26	–	310.6	0.79	0.65
	RAE-XL (Zheng et al. 2025)	800	839M	**1.13**	–	262.6	0.78	0.67
Pixel	FractalMAR-H (Li et al. 2025)	600	844M	6.15	–	348.9	0.81	0.46
	FARMER (Zheng et al. 2026)	320	1.9B	3.60	–	269.2	0.81	0.51
	EPG-XXL/16 (Lei et al. 2026)	600	789M	1.81	–	294.6	0.80	0.61
	DeCo-XL/16 (Ma et al. 2026b)	800	682M	1.62	4.41	301.0	0.80	0.62
	PixelFlow-XL (Chen et al. 2025)	320	677M	1.98	5.83	282.1	0.81	0.60
	PixNerd-XL (Wang et al. 2026)	320	700M	1.93	–	298.0	0.80	0.60
	JiT-G (Li and He 2025)	600	2B	1.82	–	292.6	0.79	0.62
	DiP-XL/16 (Chen et al. 2026b)	600	631M	1.79	4.59	281.9	0.80	0.63
	PixelGen-XL/16 (Ma, Xu, and Zhang 2026)	160	676M	1.83	–	293.6	0.79	0.63
	PixelREPA-H/16 (Shin, Kim, and Shim 2026)	600	953M	1.81	–	317.2	–	–
	FREPix-XL (Lin et al. 2026)	320	674M	1.91	–	295.6	0.79	0.62
	PixelDiT-XL (Yu et al. 2026)	320	797M	1.61	4.68	292.7	0.78	0.64
	Ours	80	798M	1.95	4.82	283.2	0.78	0.62
	Ours	260	798M	**1.52**	4.61	300.0	0.78	0.64

Table 1: **Quantitative results** on ImageNet 256×256 for class-conditioned generation.

Figure 6: **Class-conditional samples on ImageNet.** Top: samples at 512×512. Bottom: samples at 256×256.

Architecture and Implementation Details. Following the two-stage Patch–Pixel design and XL/16 configuration of PixelDiT (Yu et al. 2026), our backbone comprises a 26-block Patch-DiT encoder with hidden dimension 1152 and a four-block GL-CoDA decoder. For the Gaussian–Lanczos (G–L) observation path, we set $f_0 = 2$ and $\sigma_0 = 1$ with a fixed kernel support of 15 taps. The kernel scales are linearly annealed over flow time, and the corresponding analytic derivative is used to construct the velocity target.

Quantitative Results. Tables 1 and 2 compare our method with existing class-conditional image generators. On ImageNet 256×256, our model reaches a gFID of 1.95 after only 80 training epochs. With extended training to 260 epochs, the gFID further improves to 1.52, establishing a new state of the art among pixel-space models while using 60 fewer training epochs than the previous best. Metrics such as sFID and IS further validate this improvement, indicating that the gain in fidelity does not come at the expense of sample diversity.

Space	Method	gFID↓	sFID↓	IS↑	Precision↑	Recall↑
Latent	DiT-XL (Peebles and Xie 2023b)	3.04	5.02	240.8	0.84	0.54
	SiT-XL (Ma et al. 2024)	2.62	4.18	252.2	0.84	0.57
	MaskDiT (Zheng et al. 2023)	2.50	5.10	256.2	0.83	0.56
	U-ViT-H (Bao et al. 2023)	4.05	–	263.8	0.84	0.48
	REPA (Yu et al. 2024)	2.08	4.19	274.6	0.83	0.58
	RAE-XL (Zheng et al. 2025)	1.13	–	259.6	0.80	0.63
Pixel	PixNerd-XL (Wang et al. 2026)	2.84	5.95	245.6	0.80	0.59
	EPG-L/32 (Lei et al. 2026)	2.35	–	295.4	0.82	0.57
	JiT-H (Li and He 2025)	1.94	–	309.1	–	–
	PixelDiT-XL (Yu et al. 2026)	1.81	5.61	278.6	0.78	0.67
	DiP-XL/32 (Chen et al. 2026b)	2.31	4.48	291.7	0.84	0.58
	DeCo-XL/16 (Ma et al. 2026b)	2.22	4.67	290.0	0.80	0.60
	PixelU-H/32 (Guo et al. 2026)	1.92	5.98	322.1	0.80	0.58
	Ours	**1.58**	4.86	299.8	0.79	0.69

Table 2: **Quantitative comparison** on ImageNet 512×512.

At 512×512, our model achieves a gFID of 1.58, improving upon the previous best pixel-space result of 1.81 by 12.7%. Recall also increases from 0.67 to 0.69, suggesting improved distributional coverage alongside the lower gFID. This performance at four times the pixel count demonstrates the scalability of the proposed observation path.

Qualitative Results. Figure 6 shows representative class-conditional samples at both resolutions. At 256×256, our method yields category-faithful shapes and coherent layouts while preserving fine structures such as mushroom gills and water droplets. At 512×512, it further resolves high-frequency detail such as animal fur and weathered wood while maintaining global consistency. Together, these results show that our coarse-to-fine design reconciles semantic co-

Architecture	#params	Full-image path	G–L path
JiT	2B	4.11	**3.79**
PixelDiT	797M	2.36	**2.14**
Ours	798M	2.22	**1.95**

Table 3: **Observation-Path Ablation across Architectures, measured by FID.**

(a) Kernel		(b) Depth assignment	
Kernel	FID↓	Assignment	FID↓
Identity	2.22	Coarse only	2.28
Gaussian	2.10	Fine only	2.12
Lanczos	2.08	Fine → Coarse	2.30
G–L	**1.95**	**Coarse → Fine**	**1.95**

Table 4: **Kernel-Component and Depth-Assignment Ablations.**

herence with fine-detail fidelity across resolutions.

Ablation Study and Analysis

Depth-wise Structure Injection. Figure 7 visualizes the input features of the GL-CoDA blocks and the corresponding structural responses produced by the GL structure branch. At $t = 0.25$, the path state is heavily corrupted by noise, leaving object structures largely obscured in the block inputs. In contrast, the extracted responses exhibit a clear coarse-to-fine progression across depth: shallow blocks capture smooth global contours, while deeper blocks progressively highlight object boundaries and fine details. This behavior demonstrates that the GL structure branch extracts scale-specific structural cues from noisy intermediate representations and injects them progressively into the main feature stream.

Table 3 compares the standard full-image flow-matching path with the proposed Gaussian–Lanczos observation path across three architectures. The proposed path consistently reduces FID across all architectures, demonstrating that the benefit of scale-adaptive supervision is not specific to a particular backbone. Our Patch–Pixel backbone with GL-CoDA achieves the best performance, suggesting that time-dependent target refinement and depth-wise structural refinement provide complementary benefits.

Kernel Design and Depth Assignment. Table 4(a) ablates the components of the observation kernel. Both Gaussian and Lanczos filtering improve FID over the baseline, while their combination performs best, reducing FID to 1.95. This improvement reflects the complementary properties of the two operators: Lanczos provides sharper scale selectivity, while Gaussian smoothing attenuates its oscillatory sidelobes and reduces ringing artifacts, yielding a sharper yet cleaner coarse-scale observation.

Table 4(b) further shows that the injection order is critical. Using only coarse or only fine responses is inferior to the joint configuration, while reversing their order leads to a further performance drop. The best FID is obtained when coarse responses are assigned to shallow blocks and progressively finer responses to deeper blocks. These results show that the benefit comes not merely from introducing the structural operator, but from matching its coarse-to-fine ordering with the progression of decoder depth.

Initial kernel scales		Schedule	FID↓
Lanczos f_0	Gaussian σ_0		
4	1	Linear	2.00
2	2	Linear	2.06
2	1	Linear	**1.95**
2	1	Cosine	2.08

Table 5: **Kernel-Scale and Temporal-Schedule Sensitivity.**

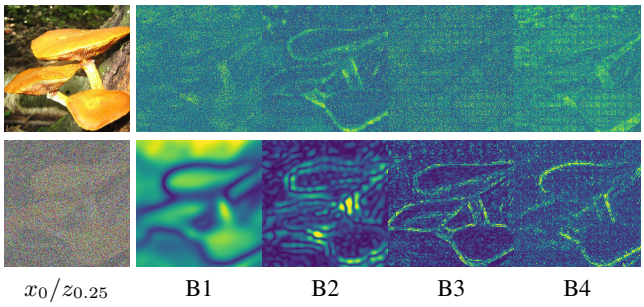

Figure 7: **Depth-wise feature visualization at $t = 0.25$.** The first column shows x_0 (top) and $z_{0.25}$ (bottom); B1–B4 show block input features (top) and our injected Gaussian–Lanczos structural responses (bottom).

Sensitivity to Scale and Schedule. Table 5 shows that, within the tested range, the model is robust to f_0 and the schedule, while being more sensitive to σ_0. Our final configuration of $f_0 = 2$, $\sigma_0 = 1$, and a linear schedule achieves the best FID of 1.95.

Conclusion

In this paper, we identify a scale–time mismatch as an overlooked source of optimization difficulty in pixel-space diffusion: image structures follow a coarse-to-fine predictability order as denoising proceeds, whereas existing models supervise all spatial scales at every step, producing low-SNR gradients that slow convergence. To address this, we propose an observation-operator diffusion framework that replaces fixed full-image supervision with a time-indexed observation trajectory, together with a path-consistent training objective. A family of Gaussian–Lanczos operators provides scale-specific observations that progressively transition from coarse structures to fine details. We further deploy these operators across decoder depth through the GL-CoDA decoder, extending the same coarse-to-fine principle from diffusion time to network depth. On ImageNet-256, our method converges faster and achieves an FID of 1.52, showing that aligning the supervised scale with the structure reliably recoverable at each denoising step improves pixel-space diffusion. Our experiments focus on natural images; extending the proposed scale-aware framework to specialized domains such as medical imaging is a promising direction for future work.

References

Bao, F.; Nie, S.; Xue, K.; Cao, Y.; Li, C.; Su, H.; and Zhu, J. 2023. All are Worth Words: A ViT Backbone for Diffusion Models. In *Proceedings of the IEEE/CVF Conference on Computer Vision and Pattern Recognition*, 22669–22679.

Burt, P. J.; and Adelson, E. H. 1983. The Laplacian Pyramid as a Compact Image Code. *IEEE Transactions on Communications*, 31(4): 532–540.

Chen, H.; Ackermann, J.; Kim, M.; Wetzstein, G.; and Guibas, L. 2026a. Asymmetric Flow Models. arXiv:2605.12964.

Chen, S.; Ge, C.; Zhang, S.; Sun, P.; and Luo, P. 2025. PixelFlow: Pixel-Space Generative Models with Flow. arXiv:2504.07963.

Chen, Z.; Zhu, J.; Chen, X.; Zhang, J.; Hu, X.; Zhao, H.; Wang, C.; Yang, J.; and Tai, Y. 2026b. DiP: Taming Diffusion Models in Pixel Space. In *Proceedings of the IEEE/CVF Conference on Computer Vision and Pattern Recognition*, 36136–36146.

Deng, J.; Dong, W.; Socher, R.; Li, L.-J.; Li, K.; and Fei-Fei, L. 2009. ImageNet: A Large-Scale Hierarchical Image Database. In *Proceedings of the IEEE Conference on Computer Vision and Pattern Recognition*, 248–255.

Dhariwal, P.; and Nichol, A. 2021. Diffusion Models Beat GANs on Image Synthesis. In *Advances in Neural Information Processing Systems*, volume 34, 8780–8794.

Fan, W.; Diao, H.; Wu, P.; and Liu, Z. 2026. Show the Signal, Hide the Noise: Spectral Forcing for Pixel-Space Diffusion. arXiv:2606.15236.

Guo, Z.; Ma, L.; He, Y.; Fu, X.; Fu, J.; Huang, J.; and Li, Y. 2026. PixelU: A U-Shaped Transformer for Efficient End-to-End Pixel Diffusion. arXiv:2606.27760.

He, Y.; Ma, L.; Guo, Z.; Shan, X.; Fu, J.; Chen, D.; Huang, J.; and Li, Y. 2026. HyperDiT: Hyper-Connected Transformers for High-Fidelity Pixel-Space Diffusion. arXiv:2605.15741.

Heusel, M.; Ramsauer, H.; Unterthiner, T.; Nessler, B.; and Hochreiter, S. 2017. GANs Trained by a Two Time-Scale Update Rule Converge to a Local Nash Equilibrium. In *Advances in Neural Information Processing Systems*, volume 30.

Ho, J.; Jain, A.; and Abbeel, P. 2020. Denoising Diffusion Probabilistic Models. In *NeurIPS*.

Hoogeboom, E.; and Salimans, T. 2022. Blurring diffusion models. *arXiv preprint arXiv:2209.05557*.

Jin, Q.; and Wang, C. 2026. Revisiting Diffusion Model Predictions Through Dimensionality. arXiv:2601.21419.

Lei, J.; Liu, K.; Berner, J.; Yu, H.; Zheng, H.; Wu, J.; and Chu, X. 2026. There Is No VAE: End-to-End Pixel-Space Generative Modeling via Self-Supervised Pre-Training. In *International Conference on Learning Representations*.

Li, T.; and He, K. 2025. Back to Basics: Let Denoising Generative Models Denoise. arXiv:2511.13720.

Li, T.; Sun, Q.; Fan, L.; and He, K. 2025. Fractal Generative Models. arXiv:2502.17437.

Lin, M.; Chen, J.; Han, L.; and Nie, L. 2026. FREPix: Frequency-Heterogeneous Flow Matching for Pixel-Space Image Generation. arXiv:2605.06421.

Lindeberg, T. 1994. *Scale-Space Theory in Computer Vision*, volume 256 of *The Springer International Series in Engineering and Computer Science*. Boston, MA: Kluwer Academic Publishers.

Lipman, Y.; Chen, R. T. Q.; Ben-Hamu, H.; Nickel, M.; and Le, M. 2023. Flow Matching for Generative Modeling. In *International Conference on Learning Representations*.

Ma, L.; Guo, Z.; He, Y.; Fu, X.; Liu, L.; Fu, J.; Huang, J.; and Li, Y. 2026a. FrequencyBooster: Full-Frequency Modeling for High-Fidelity Pixel Diffusion. arXiv:2605.17759.

Ma, N.; Goldstein, M.; Albergo, M. S.; Boffi, N. M.; Vanden-Eijnden, E.; and Xie, S. 2024. SiT: Exploring Flow and Diffusion-Based Generative Models with Scalable Interpolant Transformers. In *European Conference on Computer Vision*.

Ma, Z.; Wei, L.; Wang, S.; Zhang, S.; and Tian, Q. 2026b. DeCo: Frequency-Decoupled Pixel Diffusion for End-to-End Image Generation. In *Proceedings of the IEEE/CVF Conference on Computer Vision and Pattern Recognition*, 43600–43610.

Ma, Z.; Xu, R.; and Zhang, S. 2026. PixelGen: Improving Pixel Diffusion with Perceptual Supervision. arXiv:2602.02493.

Peebles, W.; and Xie, S. 2023a. Scalable Diffusion Models with Transformers. In *ICCV*.

Peebles, W.; and Xie, S. 2023b. Scalable Diffusion Models with Transformers. In *Proceedings of the IEEE/CVF International Conference on Computer Vision*, 4195–4205.

Rombach, R.; Blattmann, A.; Lorenz, D.; Esser, P.; and Ommer, B. 2022. High-Resolution Image Synthesis with Latent Diffusion Models. In *Proceedings of the IEEE/CVF Conference on Computer Vision and Pattern Recognition*, 10684–10695.

Shi, M.; Wang, H.; Zheng, W.; Yuan, Z.; Wu, X.; Wang, X.; Wan, P.; Zhou, J.; and Lu, J. 2025. Latent Diffusion Model without Variational Autoencoder. *arXiv preprint arXiv:2510.15301*.

Shin, J.; Kim, J.; and Shim, H. 2026. Representation Alignment for Just Image Transformers Is Not Easier Than You Think. arXiv:2603.14366.

Tong, H.; He, Y.; Li, F.; Ma, L.; Fu, J.; Chen, D.; Chen, Z.; Huang, J.; and Cao, J. 2026. Energy-Guided Flow Matching. arXiv:2608.05811.

Turkowski, K. 1990. Filters for Common Resampling Tasks. In Glassner, A. S., ed., *Graphics Gems*, 147–165. Academic Press.

Wang, S.; Gao, Z.; Zhu, C.; Huang, W.; and Wang, L. 2026. PixNerd: Pixel Neural Field Diffusion. In *International Conference on Learning Representations*.

Wang, S.; Tian, Z.; Huang, W.; and Wang, L. 2025. DDT: Decoupled Diffusion Transformer. arXiv:2504.05741.

Witkin, A. P. 1983. Scale-space filtering. *International Joint Conference on Artificial Intelligence*.

Yu, S.; Kwak, S.; Jang, H.; Jeong, J.; Huang, J.; Shin, J.; and Xie, S. 2024. Representation Alignment for Generation: Training Diffusion Transformers Is Easier Than You Think. arXiv:2410.06940.

Yu, Y.; Xiong, W.; Nie, W.; Sheng, Y.; Liu, S.; and Luo, J. 2026. PixelDiT: Pixel Diffusion Transformers for Image Generation. In *Proceedings of the IEEE/CVF Conference on Computer Vision and Pattern Recognition*, 14273–14282.

Zheng, B.; Ma, N.; Tong, S.; and Xie, S. 2025. Diffusion Transformers with Representation Autoencoders. *arXiv preprint arXiv:2510.11690*.

Zheng, G.; Zhao, Q.; Yang, T.; Xiao, F.; Lin, Z.; Wu, J.; Deng, J.; Zhang, Y.; and Zhu, R. 2026. FARMER: Flow AutoRegressive Transformer over Pixels. In *Proceedings of the IEEE/CVF Conference on Computer Vision and Pattern Recognition*, 25730–25741.

Zheng, H.; Nie, W.; Vahdat, A.; and Anandkumar, A. 2023. Fast Training of Diffusion Models with Masked Transformers. *Transactions on Machine Learning Research*.